

Depth of a strong jovian jet from a planetary-scale disturbance driven by storms

A. Sánchez-Lavega¹, G. S. Orton², R. Hueso¹, E. García-Melendo³, S. Pérez-Hoyos¹, A. Simon-Miller⁴, J. F. Rojas⁵, J. M. Gómez³, P. Yanamandra-Fisher², L. Fletcher⁶, J. Joels⁷, J. Kemerer⁸, J. Hora⁹, E. Karkoschka¹⁰, I. de Pater¹¹, M. H. Wong¹¹, P. S. Marcus¹², N. Pinilla-Alonso¹³, F. Carvalho¹⁴, C. Go¹⁵, D. Parker¹⁶, M. Salway¹⁷, M. Valimberti¹⁸, A. Wesley¹⁹ & Z. Pujic²⁰

The atmospheres of the gas giant planets (Jupiter and Saturn) contain jets that dominate the circulation at visible levels^{1,2}. The power source for these jets (solar radiation, internal heat, or both) and their vertical structure below the upper cloud are major open questions in the atmospheric circulation and meteorology of giant planets^{1–3}. Several observations¹ and *in situ* measurements⁴ found intense winds at a depth of 24 bar, and have been interpreted as supporting an internal heat source. This issue remains controversial⁵, in part because of effects from the local meteorology⁶. Here we report observations and modelling of two plumes in Jupiter's atmosphere that erupted at the same latitude as the strongest jet (23° N). The plumes reached a height of 30 km above the surrounding clouds, moved faster than any other feature (169 m s⁻¹), and left in their wake a turbulent planetary-scale disturbance containing red aerosols. On the basis of dynamical modelling, we conclude that the data are consistent only with a wind that extends well below the level where solar radiation is deposited.

Jupiter has been intensively surveyed since February 2007 using a battery of ground-based telescopes and the Hubble Space Telescope (HST) during the New Horizons spacecraft passage. Fortuitously, HST images on 25 March 2007 captured the onset of an uncommon planetary-scale disturbance in the peak of the highest speed jovian jet at 23.5° N planetographic latitude, whose eastward velocity is typically between 140 and 180 m s⁻¹ relative to the System III radio rotation period^{7–11} (Fig. 1). In the peak of the jet, a small, round bright cloud with a size of 500 km (plume B) grew rapidly, implying from mass flux conservation an average vertical velocity of ~1 m s⁻¹ (ref. 12). The second plume, plume A, emerged less than 9.26 hours later at a distance of 63,000 km (55° longitude) to the east of plume B. If plume B had triggered plume A, the required propagation velocity of the triggering mechanism would have to be 1.9 km s⁻¹ or about 1.5 times the sound speed at 6 bar. Plumes A and B moved with speeds of 169 and 164 m s⁻¹, respectively. A pattern of slower moving dark patches and bright features with velocities in the range of 100 to 150 m s⁻¹ (Fig. 2) was shed sequentially in the wake westward of both plumes, forming the north temperate belt disturbance^{13–16}. The subsequent mixing of the clouds and aerosols formed a homogeneous and redder north temperate belt (Fig. 1).

The broad wavelength coverage (from the ultraviolet at 230 nm to the thermal infrared at 20.8 µm) allowed us to retrieve the physical properties of the plumes and surrounding clouds before, during and after the disturbance. Two radiative transfer codes were used to match the plumes' reflectivity and radiance—one for the visible and near-infrared (230 nm–3 µm) to retrieve cloud properties and top altitudes, and the other for the thermal infrared (8.7–20.8 µm) to retrieve temperatures, aerosol opacity and gaseous abundances (Fig. 1e). Particles at the top of the plume heads reached the 60 ± 20 mbar level—that is, about 15 km above the tropopause (which is located between 100–150 mbar) and 30 km above the 200–400 mbar layer (where a tropospheric haze containing the cloud features seen in the visible has its greatest altitude). Above the clouds, a thin stratospheric haze with a base at 40 ± 10 mbar extends upward, but apparently the plumes did not reach this haze. The plumes had high optical thickness (above 50), and best-fitting models give bright particles with a typical radius of 7 ± 1 µm (Supplementary Information). The 200–400 mbar tropospheric haze is formed by smaller particles (about 0.5 µm). During the disturbance, the tropospheric haze increased its optical thickness from 5 ± 1 to 10 ± 2, without changing its altitude significantly, but producing redder aerosols. We therefore conclude that the plumes' tops (Fig. 1d) are formed by fresh icy particles (probably a mix of Jupiter's condensable compounds: water, ammonia and NH₄SH) injected high by the virulent upwelling, and that the disturbance increased the aerosol density and formed a red chromophore—or mixed in a pre-existing chromophore.

The high temporal sampling of our observations allowed us to track (with unprecedented resolution) the changes in the jet velocity profile associated with the disturbance at cloud level: we did this for the day the disturbance erupted (25 March), during its development (March–May) and after its cessation (5 June). (The resolution ranged from 170 to 135 km per pixel on HST frames; Fig. 2.) Disturbance features from 22° to 26° N showed zonal velocities lower than the pre-disturbed jet (Fig. 2a), while the plumes moved faster than the jet peak. We interpret the pattern as the result of instability in the strongly meridionally sheared jet triggered by the rapidly moving bright plumes. The jet became more symmetric after disturbance cessation and the peak velocity decreased by only about 15 m s⁻¹.

¹Departamento de Física Aplicada I, ETS Ingenieros, Universidad del País Vasco, Alameda Urquijo s/n, 48013 Bilbao, Spain. ²MS 169-237, Jet Propulsion Laboratory, California Institute of Technology, 4800 Oak Grove Drive, Pasadena, California 91109, USA. ³Esteve Duran Observatory Foundation, 085330 Seva, Spain. ⁴NASA Goddard Space Flight Center, Code 693, 8800 Greenbelt Road, Greenbelt, Maryland 2077, USA. ⁵Departamento de Física Aplicada I, EUITI, Universidad País Vasco, Plaza Casilla s/n, 48013 Bilbao, Spain. ⁶Atmospheric, Oceanic and Planetary Physics, Department of Physics, Clarendon Laboratory, University of Oxford, Parks Road, Oxford, OX1 3PU, UK. ⁷Principia College, 1 Maybeck Place, Elmhurst, Illinois 62028, USA. ⁸California State Polytechnic University, 3801 West Temple Street, Pomona, California 91768, USA. ⁹Harvard-Smithsonian Center for Astrophysics, 60 Garden Street, Cambridge, Massachusetts 02138, USA. ¹⁰University of Arizona, Tucson, Arizona 85721, USA. ¹¹Astronomy Department, ¹²Department of Mechanical Engineering, University of California, Berkeley, California 94720-3411, USA. ¹³Telescopio Nazionale Galileo Galilei (TNG), Roque de Los Muchachos Astronomical Observatory, 38700 Santa Cruz de La Palma, Spain. ¹⁴Centro de Estudos do Universo (CEU), 17380-000 Brotas, Brazil. ¹⁵Physics Department, University of San Carlos, Nasipit, Talamban, 6000 Cebu City, Philippines. ¹⁶Association of Lunar and Planetary Observers (ALPO), 12911 Lerida Street, Coral Gables, Florida 33156, USA. ¹⁷IcelandSpace, PO Box 9127, Wyoming, New South Wales 2250, Australia. ¹⁸Astronomical Society of Victoria, GPO Box 1059, Melbourne, Victoria 3001, Australia. ¹⁹Mathematics and Computer Science, 82 Merryville Drive, Murrumbateman 2582, Australia. ²⁰23 Attunga Street, Kingston 4114, Queensland, Australia.

(Fig. 2b, c), smaller than the change of $\sim 40 \text{ m s}^{-1}$ observed between 1979 and 2000^{7–11}. Our conclusion is that the jet remained robust against the turmoil generated by the disturbance evolution, suggesting that it extends deep below the upper clouds where motions are measured.

To test this hypothesis, we ran two different types of dynamical models. The first simulated plume formation using a three-dimensional moist convection code^{17,18} (Fig. 3a, b), exploring the atmospheric conditions that can lift the plumes to the high altitudes observed. Previous extensive simulations showed that solar water abundance and high humidities can drive storms to the tropopause but not higher¹⁷, and only if they develop in an environment that is not moist adiabatic¹⁹. To reach the 60-mbar level, we tested variations in the standard vertical temperature–pressure profile^{20,21}, and in ammonia and water abundances. A single updraft cell powered by moist water convection (cloud base level at 5–7 bar) requires 2–3 times solar water abundance with nearly 100% relative humidity and with a thermal profile 3–5 K colder than the reference temperature in the upper troposphere (at 200 mbar, Fig. 3b). The plumes might be formed by clusters of these cells²². Accordingly, the plumes are deeply rooted and extend vertically more than 120 km (from 60 mbar to 5–7 bar). Their fast zonal motion (169 and 165 m s^{-1}) reflects that of the wind at their base at 5–7 bar. Comparing the velocities at 0.3–0.4 and 5–7 bar indicates that the vertical wind shear below the upper cloud is low (increasing at about 4 m s^{-1} per scale

height of 20 km), consistent with the lifetime of the plumes. Under a strongly vertically sheared flow, our model shows that the upwelling is interrupted and the plumes do not develop. The results of the three-dimensional model were injected into a two-dimensional model reproducing the tail observed at the visible cloud level (Fig. 3c inset)²².

A second test of the vertical wind shear used the EPIC²³ general circulation model to simulate the structure and motions of the disturbance turbulent patterns (Fig. 3c). We used as an input the jet profile that was measured before the disturbance eruption (Fig. 2a). We tested the formation of the turbulent pattern by introducing a point heat source in the jet peak²⁴ on an atmospheric channel centred at the jet peak with two free parameters: the pressure level of the inflexion point where the vertical wind shear changes, and the value of this vertical wind shear. Above the clouds (from 0.6 to 0.01 bar), we assumed that the jet speed decreases as observed during the Cassini fly-by²¹. The formation of the turbulent pattern is very sensitive to the jet shape at cloud level. We tested this sensitivity by performing the numerical simulations with wind profiles measured at different epochs. Among them, the Cassini wind profile¹¹ and the 5 June HST profile were stable against the heat source perturbation. On the contrary, the jet profile we measured on the outbreak day (Fig. 2a) becomes rapidly unstable as we introduce the perturbation. Moreover, the disturbance pattern resembles the observed one when the inflexion point is at a pressure of 600 mbar (at the predicted

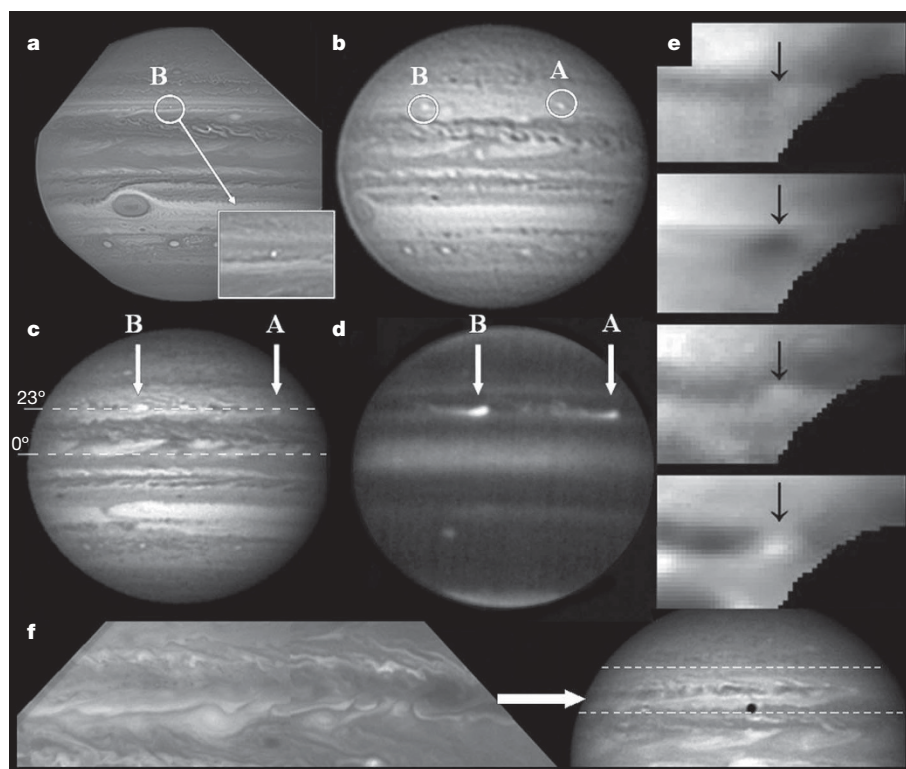


Figure 1 | Plume onset, growth and disturbance development (March–May 2007). **a**, Onset of plume B, 25 March (HST, 410 nm). **b**, Growth of plumes A and B, 27 March (IOPW, visible). Both plumes grew in ~ 1.3 days to a size of 2,000 km. Plume A was at $23.4^\circ \pm 0.5^\circ \text{ N}$ and moved with a speed of $169.2 \pm 0.5 \text{ m s}^{-1}$, and plume B was at $23.1^\circ \pm 0.5^\circ \text{ N}$ and moved with a speed of $164.3 \pm 1.7 \text{ m s}^{-1}$ (see Supplementary Information). **c**, Plumes and disturbances in their wake, 5 April (IOPW, visible). Both plumes were bright features in the visible (meridional extent of 2,500 km, 4,000 km zonal) and particularly prominent at wavelengths sensitive only to high-altitude levels. **d**, Plumes and their tails retrieved at high altitude (NASA-IRTF, $2.3 \mu\text{m}$ methane filter). **e**, Maps of plume A observed in the thermal infrared on 5 April (IRTF). These excerpts from cylindrical maps show the deviation from the zonal mean of the indicated parameters in the plume head region (top to bottom): temperature at 123.4 mbar, temperature at 393 mbar, aerosol

content above 600 mbar and ammonia abundance near 300 mbar. The plume produced lower temperatures near 392.9 mbar, but marginally higher temperatures at 123 mbar, as well as increased ammonia–cloud level aerosols and 300-mbar ammonia gas abundances. The arrows mark the plume head region. **f**, Turbulence and wavy patterns in the wake of plume A followed by the formation of a new north temperate belt as observed on 1 May by the Hubble Space Telescope (left, 410 nm, magnified view) and IOPW observers (right; the horizontal bars limit the area of the north temperate belt). The HST image shows the turbulent pattern formed at latitudes 20 – 28° N , with a predominant wavelength of 7,000–12,000 km. Plume B disappeared around the time the dark patches shed by plume A reached the location of plume B in about 14 days. The disturbance advanced to the west, encountering plume A on its eastern side on 11 May (its lifetime was 45 days), when it disappeared.

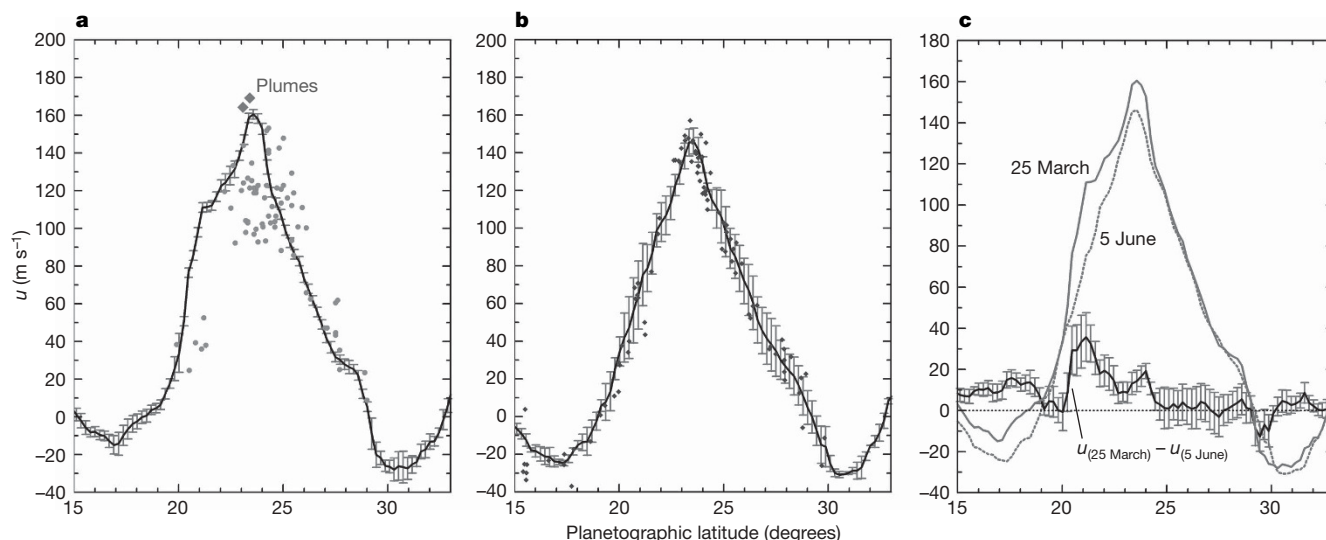


Figure 2 | Time dependence of the profile of the north temperate jet.

a, Zonal velocity of the disturbance features (filled circles) and plumes A and B (filled diamonds) between 25 March and 31 May 2007 measured by cloud tracking, as compared to the profile the day of the eruption (continuous line, pre-disturbance stage on 25 March 2007) obtained by one-dimensional zonal brightness correlation on HST images (error bars represent the standard deviation of the measurements). **b**, Jet profile after the disturbance

ended, 5 June 2007. The continuous line represents the profile obtained by zonal correlation and the dots by cloud tracking, both on HST images (error bars represent the standard deviation of the measurements). **c**, Comparison of the jet profiles before the eruption (25 March 2007) and after the disturbance end (5 June 2007). The difference between both profiles as a function of latitude is shown as a darker line with associated error bars representing the standard deviation of the measurements.

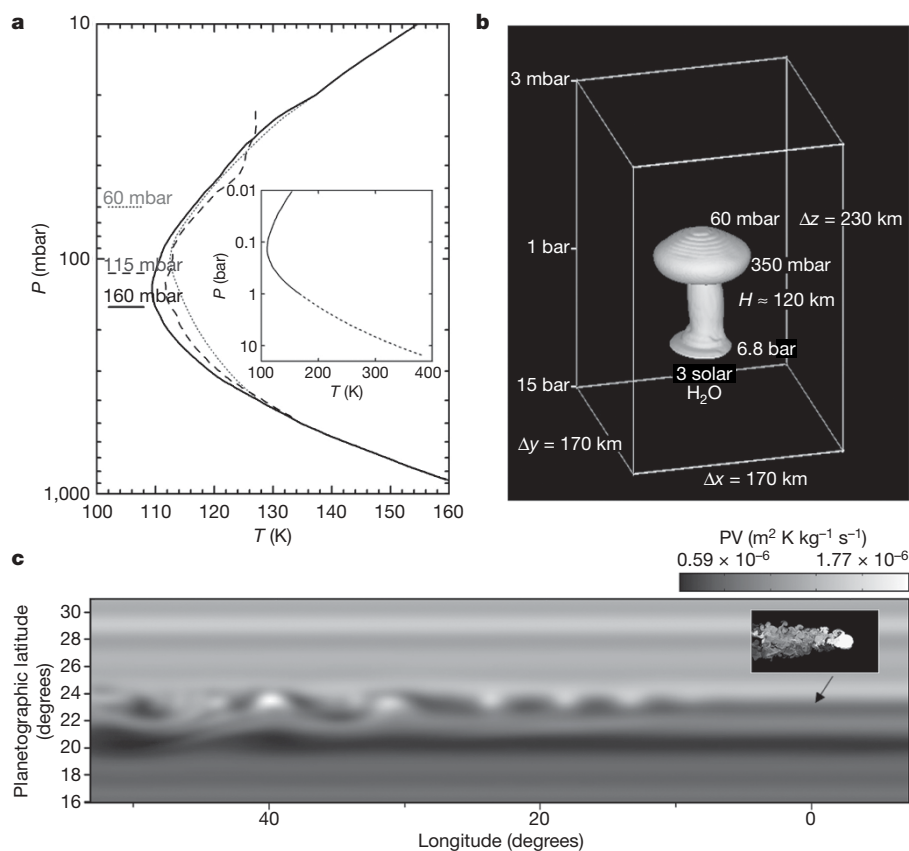


Figure 3 | Models of the plume onset and disturbance development.

a, b, Wet convective three-dimensional model of the plumes. **a**, Thermal profiles used to run the simulations and the cloud top level reached by the convective cell assuming a deep water content of 3 times solar abundance and 95% of relative humidity above the condensation level. P , pressure; T , temperature. The continuous line corresponds to the Cassini CIRS thermal profile at the NTB location¹⁹, the dashed line to the Voyager IRIS thermal profile¹⁸ and the dotted line to a synthetic profile with less static stability from 500 to 200 mbar required for the storms to reach the 60 mbar level. The inset shows the wet adiabat extension deep in the atmosphere. **b**, Convective

cell resulting from the model able to fit the observed cloud tops of the plumes and the domain of simulation. **c**, The plume brightness distribution (inset) results from a two-dimensional model of a round cloud placed in the peak of the jet and evolving as it interacts with the meridional shear of the zonal wind¹⁷ with a spatial resolution of 5 km over a $10,000 \times 5,000$ km area. The map (main panel) shows the distribution of Ertel's potential vorticity (PV; greyscale) at 650 mbar after 30 days for a simulation where the jet extends vertically downwards with constant value from the upper cloud layer at altitude ~ 0.6 bar down to at least 5–7 bar (the location of the water clouds and the plume source). Inset and map are at the same scale.

ammonia cloud level) and the vertical wind shear down from this altitude to the water cloud base at 5–7 bar is zero or increases slightly with depth. This result reinforces the conclusion that the jet extends with low vertical wind shear down along the whole ‘weather layer’ to at least the 5–7 bar pressure level.

Our 5–7 bar zonal wind speed of $169\text{--}165\text{ m s}^{-1}$ at 23° N is consistent with the 180 m s^{-1} velocity determined for that depth by the Galileo probe⁴ at 7° N , as well as the 240 m s^{-1} wind speed from previous EPIC simulations of the long-term behaviour of the 1990 disturbance²⁴. These studies agree that the winds do not decay below the upper ammonia cloud, and extend deeper than the solar radiation penetration level at 1–2 bar (see Supplementary Information), in agreement with previous ideas on the depth and stability of the jovian jet structure²⁵.

A comparison of this disturbance with two previous events in 1975 and 1990 suggests additional caveats and surprising similarities^{13,14}: first, the outburst occurred with an interval of $\sim 15\text{--}17$ years; second, the plumes always appear in the jet peak within $\pm 0.5^\circ$; third, the disturbance erupted with two plumes (not one, three or more); fourth, the eastern plume, located in longitude east of the other (taking as a reference the shortest distance between both) is always the fastest; and last, the plumes moved with a speed in the range $\sim 165\text{--}170\text{ m s}^{-1}$ in all three events.

Received 30 July; accepted 29 November 2007.

- Ingersoll, A. P. *et al.* in *Jupiter: The Planet, Satellites & Magnetosphere* Ch. 6 (eds Bagenal, F., McKinnon, W. & Dowling, T.) 105–128 (Cambridge Univ. Press, Cambridge, 2004).
- Sánchez-Lavega A., Hueso, R., Pérez-Hoyos, S., García-Melendo, E. & Rojas, J. F. in *Lecture Notes and Essays in Astrophysics* Vol. I (eds Ulla, A. & Manteiga, M.) 63–85 (Universidad de Vigo, Vigo, Spain, 2004).
- Vasavada, A. R. & Showman, A. P. Jovian atmospheric dynamics: An update after Galileo and Cassini. *Rep. Prog. Phys.* **68**, 1935–1996 (2005).
- Atkinson, D. H., Pollack, J. B. & Seiff, A. The Galileo probe Doppler wind experiment: Measurement of the deep zonal winds on Jupiter. *J. Geophys. Res.* **103** (E10), 22911–22928 (1998).
- Showman, A. P., Gierasch, P. J. & Lian, Y. Deep zonal winds can result from shallow driving in a giant-planet atmosphere. *Icarus* **182**, 513–526 (2006).
- Showman, A. P. & Dowling, T. E. Nonlinear simulations of Jupiter’s 5-micron hot spots. *Science* **289**, 1737–1740 (2000).
- Maxworthy, T. The dynamics of a high-speed jovian jet. *Planet. Space Sci.* **32**, 1053–1058 (1984).
- Limaye, S. S. Jupiter – New estimates of the mean zonal flow at the cloud level. *Icarus* **65**, 335–352 (1986).
- Simon, A. A. The structure and temporal stability of Jupiter’s zonal winds: A study of the north tropical region. *Icarus* **141**, 29–39 (1999).
- García-Melendo, E. & Sánchez-Lavega, A. A study of the stability of Jovian zonal winds from HST images: 1995 – 2000. *Icarus* **152**, 316–330 (2001).
- Porco, C. C. *et al.* Cassini imaging of Jupiter’s atmosphere, satellites, and rings. *Science* **299**, 1541–1547 (2003).
- Sánchez Lavega, A. & Battaner, E. The nature of Saturn’s atmospheric Great White Spots. *Astron. Astrophys.* **185**, 315–326 (1987).
- Sánchez-Lavega, A. & Quesada, J. A. Ground-based imaging of Jovian cloud morphologies and motions. II. The northern hemisphere from 1975 to 1985. *Icarus* **76**, 533–557 (1988).
- Sánchez-Lavega, A., Miyazaki, I., Parker, D., Laques, P. & Lecacheux, J. A disturbance in Jupiter’s high-speed north temperate jet during 1990. *Icarus* **94**, 92–97 (1991).
- Peek, B. M. *The Planet Jupiter* (Faber & Faber, London, 1958).
- Rogers, J. H. *The Giant Planet Jupiter* (Cambridge Univ. Press, Cambridge, UK, 1995).
- Hueso, R. & Sánchez-Lavega, A. A three-dimensional model of moist convection for the giant planets: The Jupiter case. *Icarus* **151**, 257–274 (2001).
- Hueso, R. & Sánchez-Lavega, A. A three-dimensional model of moist convection for the giant planets II: Saturn’s water and ammonia moist convective storms. *Icarus* **172**, 255–271 (2004).
- Nakajima, K., Takehiro, S. I., Ishiwatari, M. & Hayashi, Y. Y. Numerical modeling of Jupiter’s moist convection layer. *Geophys. Res. Lett.* **27**, 3129–3132 (2000).
- Lindal, G. F. *et al.* The atmosphere of Jupiter: An analysis of the Voyager radio occultation. *J. Geophys. Res.* **86**, 8721–8727 (1981).
- Simon-Miller, A. A. *et al.* Jupiter’s atmospheric temperatures: From Voyager IRIS to Cassini CIRS. *Icarus* **180**, 98–112 (2006).
- Hueso, R., Sánchez-Lavega, A. & Guillot, T. A model for large-scale convective storms in Jupiter. *J. Geophys. Res.* **107**, doi:10.1029/2001JE001839 (2002).
- Dowling, T. E. *et al.* The explicit planetary isentropic-coordinate (EPIC) atmospheric model. *Icarus* **132**, 221–238 (1998).
- García-Melendo, E., Sánchez-Lavega, A. & Dowling, T. E. Jupiter’s 24° N highest speed jet: Vertical structure deduced from nonlinear simulations of a large-amplitude natural disturbance. *Icarus* **176**, 272–282 (2005).
- Dowling, T. E. Estimate of Jupiter’s deep zonal-wind profile from Shoemaker-Levy 9 data and Arnold’s second stability criterion. *Icarus* **117**, 439–442 (1995).

Supplementary Information is linked to the online version of the paper at www.nature.com/nature.

Acknowledgements We thank all the contributors to the International Outer Planet Watch (IOPW) observing programme for their efforts in the Jupiter imaging survey. This work was supported by the MEC PNAYA, Grupos UPV, CESCA (Barcelona) and Fondos FEDER. R.H. was supported by the ‘Ramón y Cajal’ programme. We acknowledge the HST director’s discretionary times. G.S.O. and P.Y.-F. were visiting astronomers at the IRTF, supported by the University of Hawaii and NASA.

Author Information Reprints and permissions information is available at www.nature.com/reprints. Correspondence and requests for materials should be addressed to A.S.-L. (agustin.sanchez@ehu.es).

CORRIGENDUM

doi:10.1038/nature06807

Depth of a strong jovian jet from a planetary-scale disturbance driven by storms

A. Sánchez-Lavega, G. S. Orton, R. Hueso, E. García-Melendo, S. Pérez-Hoyos, A. Simon-Miller, J. F. Rojas, J. M. Gómez, P. Yanamandra-Fisher, L. Fletcher, J. Joels, J. Kemerer, J. Hora, E. Karkoschka, I. de Pater, M. H. Wong, P. S. Marcus, N. Pinilla-Alonso, F. Carvalho, C. Go, D. Parker, M. Salway, M. Valimberti, A. Wesley & Z. Pujic

Nature 451, 437–440 (2008)

In Fig. 3a, the descriptions of the continuous and dotted curves were inadvertently swapped. The continuous line corresponds to the modified synthetic thermal profile (storms reaching the 60 mbar level). The dotted line corresponds to the Cassini CIRS thermal profile (storms reaching the 160 mbar level).

ERRATUM

doi:10.1038/nature06729

Roquin represses autoimmunity by limiting inducible T-cell co-stimulator messenger RNA

Di Yu, Andy Hee-Meng Tan, Xin Hu, Vicki Athanasopoulos, Nicholas Simpson, Diego G. Silva, Andreas Hutloff, Keith M. Giles, Peter J. Leedman, Kong Peng Lam, Christopher C. Goodnow & Carola G. Vinuesa

Nature 450, 299–303 (2007)

In this Letter, some axis labels in Figs 3 and 4 were inadvertently mislabelled. In Fig 3d, the labels on the *x* axes of the three graphs should read 'Hi Low Nil' instead of 'Hi Low Ni'. The *x* axes of the bar graphs in Fig. 4a (right and left panels) and Fig. 4b (right panel) should read 'Hi Low Nil' instead of 'Hi Low Hi'.

CORRIGENDUM

doi:10.1038/nature06728

The nonlinear Fano effect

M. Kroner, A. O. Govorov, S. Remi, B. Biedermann, S. Seidl, A. Badolato, P. M. Petroff, W. Zhang, R. Barbour, B. D. Gerardot, R. J. Warburton & K. Karrai

Nature 451, 311–314 (2008)

The experiment measures the differential laser transmission through the quantum dot between the on- and off-exciton resonance condition. As a result, the origin in Fig. 2a–h corresponds to the zero of the measured differential transmission and does not exclude the existence of constant background absorption. It is therefore important to note that the undershoot in the Fano spectra does not correspond to a negative absorption (that is, an optical gain), but is consistent with the continuum broadband background absorption, as analysed in our observation of the nonlinear Fano effect. Similarly, the theoretical graphs in Fig. 2i–n are also given for the differential transmission.

CORRIGENDUM

doi:10.1038/nature06779

Systems biology approaches identify ATF3 as a negative regulator of Toll-like receptor 4

Mark Gilchrist, Vesteinn Thorsson, Bin Li, Alistair G. Rust, Martin Korb, Jared C. Roach¹, Kathleen Kennedy, Tsonwin Hai, Hamid Bolouri & Alan Aderem

¹Institute for Systems Biology, Seattle, Washington 98103, USA.*Nature* 441, 173–178 (2006)

In this Article, Jared C. Roach was inadvertently omitted from the list of authors. He was responsible for designing the immune-specific array for ChIP-to-chip analysis. J.C.R. received support from the National Institute of Allergy and Infectious Diseases, National Institutes of Health.